JEE Journal of Ecological Engineering

Journal of Ecological Engineering 2024, 25(4), 66–79
https://doi.org/10.12911/22998993/183649
ISSN 2299–8993, License CC-BY 4.0

Received: 2024.01.23
Accepted: 2024.02.12
Published: 2024.03.01

Novel Supported Ionic Liquid Adsorbents for Hydrogen Sulphide Removal from Biogas

Norsyahira Saffiee[1], Muhammad Zulhaziman Mat Salleh[1,2], Wan Nor Roslam Wan Isahak[1,2], Fatihah Suja[3], Gong Tao Ding[4], Sureewan Sittijunda[5], Peer Mohamed Abdul[1,2*]

[1] Department of Chemical and Process Engineering, Faculty of Engineering and Built Environment, Universiti Kebangsaan Malaysia, 43600 Bangi, Selangor, Malaysia

[2] Research Centre for Sustainable Process Technology (CESPRO), Faculty of Engineering and Built Environment, Universiti Kebangsaan Malaysia, 43600 Bangi, Selangor, Malaysia

[3] Department of Civil Engineering, Faculty of Engineering and Built Environment, Universiti Kebangsaan Malaysia, 43600 Bangi, Selangor, Malaysia

[4] Biomedical Research Centre, Northwest Minzu University, Gansu Lanzhou, 730030, China

[5] Faculty of Environment and Resource Studies, Mahidol University, Nakhon Pathom, 73170, Thailand

* Corresponding author's e-mail: peer@ukm.edu.my

ABSTRACT

The imidazolium-based supported ionic liquids (IL) in activated carbon (AC) is an exciting strategy for developing new adsorbents for H_2S removal from biogas. In this work, the influence of IL on AC was discovered by examining the effect of ultrasonic stirring as an impregnation method, AC particle size and IL anion type. AC300µm-[Bmim]Cl-U5 demonstrated the highest H_2S adsorption capacity of 8.25±0.38 mg H_2S/g and was obtained through [Bmim]Cl impregnated on 300 µm AC size through the ultrasonic stirring for five minutes at room temperature. The adsorption/desorption study confirmed the regeneration ability of AC300µm-[Bmim]Cl-U5 up to three cycles with a maximum adsorption capacity of 14.24±0.43 mg H_2S/g. The SEM images confirmed the presence of IL on the AC surface and were further explained through BET analysis. TGA measurement indicated the thermal stability of pristine IL, the fresh and exhausted adsorbent. Therefore, this study proved the potential of ultrasonic-assisted supported IL as a promising adsorbent for H_2S removal from biogas that exhibits excellent properties in high adsorption capacity and thermal stability.

Keywords: biogas, hydrogen sulphide, ionic liquids, gas adsorption.

INTRODUCTION

Biogas produced via anaerobic digestion stands out as a highly promising renewable energy source, readily available in many countries, including Malaysia (Syahri et al., 2022). The composition of produced biogas varies depending on the feedstock, such as municipal, agricultural, and kitchen waste (Prasad et al., 2017). Typically, methane (CH_4) dominates biogas composition, accounting for 60–70%, followed by carbon dioxide (CO_2) at 30–40% (Al Mamun and Torii, 2015; Amin et al., 2022; Chaemchuen et al., 2016; Korbag et al., 2021). However, the anaerobic digestion process that generates biogas produces hydrogen sulphide (H_2S), a highly toxic, poisonous, and corrosive gas (Zulkefli et al., 2022a). To prevent environmental emissions, H_2S must be removed, and various technologies such as adsorption, absorption, membrane separation, and molecular sieve are available for this purpose (Andriani et al., 2020; Xiao, 2017).

Chemical absorption, utilising amine, carbonate, and ammonia solvents as absorbents, is a well-established and effective method for H_2S removal. However, the application of chemical

solvents is constrained by the concerns related to physical characteristic limitations, such as viscosity, corrosiveness, and higher energy consumption (Choi et al., 2014). Ionic liquids (IL) emerge as a promising solvent for H_2S removal, being vapourless, thermally stable, reusable, and recognised as environmentally friendly solvents (Beigi et al., 2018). IL exist in a liquid form as molten salts and are composed of both anions and cations. Examples of cations include imidazolium, ammonium, phosphonium, pyridinium, and pyrrolidinium, while anions include tetrafluoroborate, hexafluorophosphate, bistrifluorosulfonylimide, and chloride. ILs are often referred to as 'designer' solvents due IL to their unique ability to fine-tune physicochemical properties by slightly modifying the structure of corresponding anions and cations (Taheri et al., 2021).

Besides absorption, adsorption emerges as a notably simple process, a technology with easy operation and low energy consumption, particularly well-suited for small-scale applications (Zhang H.Y. et al., 2019). While activated carbon (AC) serves as a common, cost-effective, and readily available adsorbent material, it encounters challenges regarding selectivity, breakthrough time, and limited capacity (Nurhidayah et al., 2022; Lucena et al., 2020; Plaza et al., 2010). On the other hand, IL possess issues like viscosity, high cost and dynamic separation (Bárbara Burlini Polesso et al., 2019). Combining AC and IL, however, presents an increasingly effective adsorbent solution with high adsorption capacity performance. This approach addresses the flaws of both materials and minimises IL usage, employing only a low percentage for AC-IL impregnation.

This study aimed to combine the advantages of AC with the unique properties of IL using an ultrasonic-assisted stirring method. This approach provides a new idea of a novel and greener technique for effective H_2S removal. Previous methods of conventional stirring supported-IL were time-consuming, with required duration ranging from two to six hours (Huang et al., 2022; Ren et al., 2023). Hence, the effect of ultrasonic stirring time was studied to determine the ideal time of IL impregnation on AC. However, the pore size of the adsorbent has also been a critical issue. Previous studies of supported IL adsorbent focused more on the mesoporous material of silica and alumina (Duczinski et al., 2018; Bárbara B. Polesso et al., 2019; Bárbara Burlini Polesso et al., 2019). Hence, two AC particle sizes of 300 and 600 µm were chosen as IL support further to investigate the particle size effect on H_2S removal. Lastly, the IL character of different anions was investigated through the hydrophilic IL of [Bmim]Cl and hydrophobic IL of [Bmim][NTf_2]. The hydrophobic/hydrophilic nature of IL was believed to significantly affect selective gas removal (Caglayan et al., 2023). However, limited investigation has been conducted in this regard. Hence, [Bmim]Cl and [Bmim]NTf_2 were opted in this work as promising candidates for H_2S adsorption. Furthermore, the high solubility of both IL, as examined in previous works, is believed to contribute to their performance as effective adsorbents (Cheng et al., 2021; Guanhua et al., 2019; Mutalib et al., 2022; Bárbara B. Polesso et al., 2019; Zhou et al., 2016). Therefore, the interaction between IL and H_2S and the influence of IL solubility on the H_2S adsorption capacity were further evaluated using COSMO-RS. The outcomes propose the best AC and IL selection for the ultrasonic-assisted adsorbent and contribute to a deeper understanding of the fundamental interaction between IL and H_2S to enhance H_2S gas removal efficiency, specifically from biogas.

EXPERIMENTS

Materials

The coconut husk-AC with a mesh size of 20×40 was used in this study. High purity of 98% IL of [Bmim]Cl and [Bmim][NTf_2] were purchased from Sigma Aldrich. The gas tank containing a mixture of 2000 ppm H_2S/N_2 was obtained from Alpha Gas Solution. A column 10/10 from Cytiva was purchased and used as the adsorption column. Gas concentration was measured using Biogas Analyzer Geotech GA 5000 from QED Environmental Systems. The schematic diagram of the adsorption system setup is illustrated in Figure 1.

Supported IL preparation

The AC was sieved to achieve 300 and 600 µm uniform particle sizes. Next, the AC was dried at 90 °C for 24 hours to eliminate the moisture and stored in an airtight bottle before use. Adsorbent preparation was started with the dilution of 0.20 g of [Bmim]Cl in 10 ml of ethanol. The solution

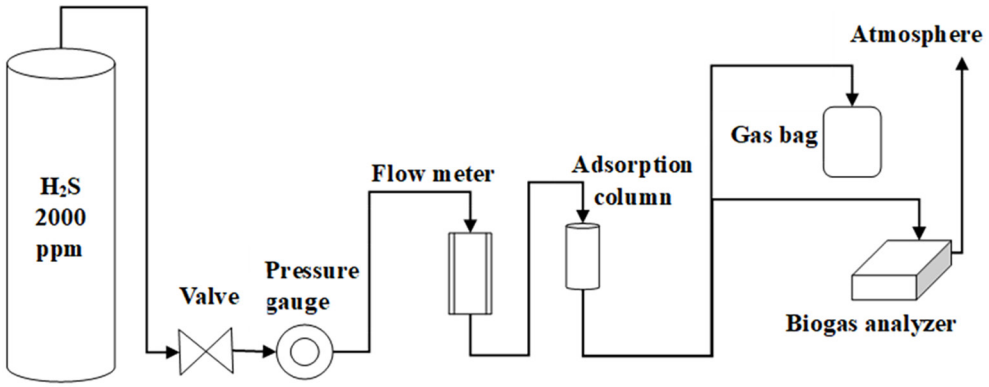

Figure 1. Schematic diagram of adsorption experiment system

was allowed to dissolve for a few minutes before being added to a universal bottle filled with 2.0 g of AC. The AC-IL solution was then subjected to ultrasonic stirring at 50 Hz for 0, 5, 10, 20, and 30 minutes at room temperature. Then, the ethanol was removed using a rotary evaporator at 75°C. Lastly, the AC-IL adsorbent was dried at 90°C for 24 hours in an oven to remove excess solvent. These procedures were replicated for different AC particle sizes and IL. Each adsorbent sample was labelled ACXμm-[IL]-UY, where X represents AC particle size (300, 600), and Y denotes the ultrasonic duration in minutes.

H_2S adsorption and desorption

Approximately 2.00 g of absorbent was measured and packed with glass wool in a column with 10 × 10 mm (length x inner diameter). The adsorption tests were conducted at ambient temperature and pressure (1 bar). The fed concentration was 2000 ppm H_2S diluted in N_2 and flowed at 0.10 L/min. The adsorption time and outlet concentration were recorded for each five minutes until the breakthrough and saturation points (for adsorption/desorption tests). A Geotech GA 5000 biogas analyser was used to measure the real-time H_2S outlet concentration. The adsorption/desorption test was carried out using the optimum adsorbent under the same conditions (room temperature and 1 bar) for three cycles. The exhausted sample was heated at 150 °C for 30 minutes to desorb the gas before each cycle. Each test was duplicated for better accuracy. Next, the H_2S adsorption capacities of supported IL-AC adsorbents were calculated at one ppm (as the breakthrough time). T_B and C values were recorded in minutes and ppm, respectively, and applied as in Equation 1 (Zulkefli et al., 2022a):

$$q = \frac{Q \times T_B \times C_0 \times MW_{H_2S}}{V_m \times m_{adsorbent} \times 10^6} \quad (1)$$

where: q is referred to adsorption capacity (mg H_2S/g), Q is the flow rate (L/min), T_B is the breakthrough time at one ppm (min), C_0 is the H_2S gas concentration (ppm), MW_{H2S} is H_2S molecule mass (mg/mol), V_m is the molar volume at S.T.P (L/mol), and $m_{adsorbent}$ is the final mass of AC-IL sample (g).

The maximum adsorption capacity, Q_{max} of the adsorbent in each cycle was calculated as in Equation 2, as modified from Equation 1:

$$Qmax = \frac{Q \times T_B \times C \times MW_{H_2S}}{V_m \times \left(\frac{m_{final} - m_{initial}}{m_{final}}\right) \times 10^6} \quad (2)$$

where: m_{final} is the mass of exhausted adsorbent, $m_{initial}$ is the mass of desorbed absorbent.

The degradation of each cycle was calculated as the percentage differences as in Equation 3 (Zulkefli et al., 2022a), where N is the previous cycle and N+1 is the current cycle.

$$Degradation\ (\%) = \frac{Q_{maxN} - Q_{maxN+1}}{Q_{maxN}} \times 100 \quad (3)$$

The adsorbent performance was calculated as the removal efficiency as in (Kalidhasan et al., 2012), when C_{inlet} and C_{outlet} are referred to inlet and outlet H_2S concentration in ppm.

$$Efficiency\ (\%) = \frac{C_{inlet} - C_{outlet}}{C_{inlet}} \times 100 \quad (4)$$

Characterisation of the adsorbent

X-ray diffraction (XRD) analyses of the fresh and exhausted (after H_2S exposure) adsorbents were performed using Bruker D8 Advance, with Cu Kα (40 kV, 40 mA) at λ = 0.154 nm and

range temperature of 256–2054 °C. On the basis of Bragg's Law, XRD powder patterns (~10 mg) were shown in the 2θ range of 5–80°. Scanning Electron Microscopy (SEM) analyses using ZEISS Supra 55VP determined the sample morphology and elemental content. The structure of the sample surface can be portrayed at 10x to 300Kx magnification with a maximum of 10nm of sample thickness. Brunauer–Emmett–Teller (BET) theory in Micrometritics TriStar II Plus version 3.03 was applied to calculate the specific surface area and porosity based on nitrogen adsorption/desorption isotherm at 77 K. Around 0.20 g of sample were placed under nitrogen flow at 250 ℃ for three hours. The surface area, pore volume, and pore size were calculated by the BET as well as Barrett–Joyner–Halanda (BJH) at p/p_0 = 0.95. Thermal gravimetric analysis (TGA) data were obtained through the NETZSCH STA 449 F3 Jupiter model. The samples were heated from 30–600 ℃ at 20 ℃/min under 20 ml/min nitrogen flow. Before the measurement, the sample of <5.0 mg was pre-treated at 120℃ for two hours in the oven to remove the moisture.

Computational study of COSMO-RS

COSMO-RS was used to predict the thermodynamic properties and interaction behaviour of H_2S and IL upon mixing. It was assumed that the absorption performance could be correlated with the solubility of H_2S in IL, based on the fugacity of H_2S molecules in vapour and liquid phases, as described by Henry's law. The solubility values of H_2S in various ILs were gathered from the current study and existing literature to benchmark the accuracy of the COSMO-RS model. Imidazolium-based IL, such as 1-hexyl-3-methylimidazolium [Hmim], 1-butyl-3-methylimidazolium [Bmim], and 1-ethyl-3-methylimidazolium [Emim] paired with different halide anion such as BF_4^-, NTf_2^- and Cl^- were explored based on prior research. Examples of the IL involved in this study encompass [Bmim][Cl] (Zhou et al., 2016), [Bmim][NTf_2] (Jalili et al., 2009), [Hmim][NTf_2] (Rahmati-Rostami et al., 2009), [Emim][NTf_2] (Huang et al., 2016; Sakhaeinia et al., 2010), [Hmim][BF_4] (Huang et al., 2016; Rahmati-Rostami et al., 2009) and [Emim][BF_4] (Jalili et al., 2019). The collected data from this investigation and the literature served to cross-check and validate the predictive capabilities of the COSMO-RS model.

Thermodynamic properties of the mixtures were calculated based on the generated and optimised molecular structure of the species involved, which is imported into COSMOtherm as the *.cosmo file*. The generation of the *.cosmo file* was conducted through a single-point calculation using DFT with Becke–Perdew and the Triple-ζ Zeta Valence Potential (TZVP) basis set. The solubility of H_2S in each IL was predicted under 1 bar pressure and calculated using COSMO-RS based on Equation 5 (Fariza et al., 2022):

$$p_{H2S} = p^0_{H2S} \cdot x_{H2S} \cdot \gamma_{H2S} \quad (5)$$

where: pH_2S is the partial pressure and p^0H_2S is the vapor pressure of the pure H_2S; xH_2S is the mole fraction and γH_2S is the activity coefficient of H_2S (Balchandani and Singh, 2021). The solubility values are calculated as a mole fraction of H_2S in the liquid phase and recorded in mol/kg.

RESULTS AND DISCUSSION

Effect of ultrasonic stirring time on H_2S removal

AC, with a particle size of 300 μm (AC300μm), serves as the solid material for the impregnation of [Bmim]Cl facilitated by ultrasonic stirring. Ultrasonic stirring is chosen for its capability to provide uniform and effective stirring as well as further enhance the adsorption efficiency (Mullick and Neogi, 2019). The effect of ultrasonic stirring time was systematically investigated across durations of 0, 5, 10, 20, and 30 minutes at room temperature. As depicted in Figure 2, the most significant H_2S adsorption capacity was achieved within a short 5-minute ultrasonic impregnation through the sample designated as AC300μm-[Bmim]Cl-U5. AC300μm-[Bmim]Cl-U5 exhibited highest adsorption capacity of 8.25±0.38 mg H_2S/g. The efficiency of ultrasonic stirring lies in its ability to promote the opening of additional micropores within the AC structure, thereby increasing the surface area for interaction between AC and the IL. It is noteworthy that prolonged stirring times resulted in lower adsorption capacities due to the possibility of AC pore blockage, which reduces the available surface area (Zhang et al., 2018). The shorter stirring time proves advantageous for mass transfer as rapid formation of microbubbles and loss facilitate the process. In addition, Dou et al. (2016) used ultrasonic-assisted

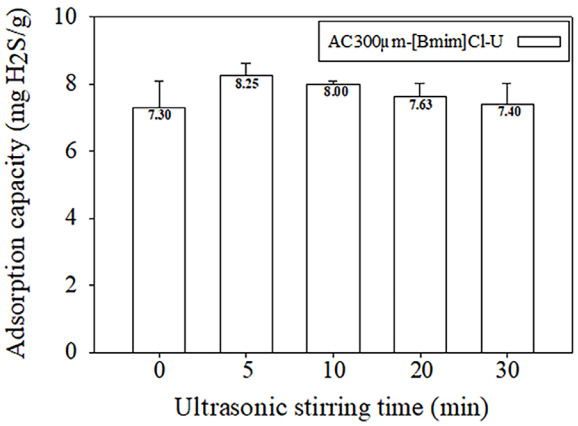

Figure 2. H_2S adsorption capacity of AC300-[Bmim]Cl at different ultrasonic stirring time sizes under ambient temperature and pressure

stirring to impregnate Fe-Zn-Cu in char for simultaneous removal of H_2S and CO_2. The findings prove the ultrasonic stirring increased the surface area and pore volume, contributing up to 17.62 g S/100 g adsorption capacity (Dou et al., 2015). This also agrees with the previous studies by Jiang et al. (2020) and Zhang et al. (2019), both found that ultrasonic stirring can increase the AC surface area and pores.

Effect of AC particle size on H_2S removal

The effect of AC particle size was studied using [Bmim]Cl impregnated on AC using ultrasonic stirring for 5 minutes at room temperature. Figure 3a shows the H_2S adsorption capacity of AC-[Bmim]Cl-U5 at different sizes, 300 and 600 µm AC. It demonstrates that AC with a smaller particle size possesses a greater capacity for gas adsorption than its larger counterparts. Figure 3b shows the breakthrough curves obtained at ambient temperature and pressure at 0.10 L/min flow rate. The breakthrough time increases at decreasing AC particle size, consistently with the higher adsorption capacity, according to the data presented in Figure 3b (Santiago et al., 2019). AC600µm-[Bmim]Cl-U5 demonstrated a shorter breakthrough time of 58.5 minutes than AC300µm-[Bmim]Cl-U5 while achieving 88.15% removal efficiency at 105 minutes (Dou et al., 2016). Smaller particle size facilitates better dispersion of IL through increased surface area to volume ratio of the adsorbent (Zulkefli et al., 2022b). On the basis of the BET analysis conducted on raw AC (without impregnation) presented in Table 1, a smaller AC particle, AC300µm, possesses a higher surface area and total pore volume than AC600µm, which gives more exposed sites on the particle where adsorption can occur.

Effect of IL anion type on H_2S removal

Figure 4a and Figure 4b demonstrated the H_2S adsorption capacity of AC300-U5 with the impregnation of [Bmim]Cl and [Bmim]NTf_2. As it can be observed in Figure 4a, AC300µm-[Bmim]Cl-U5 exhibits much greater H_2S adsorption

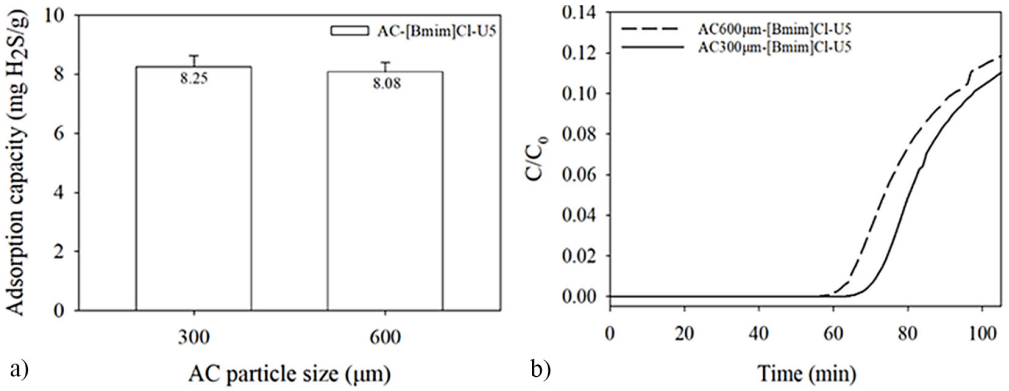

Figure 3. (a) H_2S adsorption capacity and (b) breakthrough curve of AC-[Bmim]Cl-U5 at different particle sizes under ambient temperature and pressure

Table 1. Pore properties of raw AC

AC particle size (µm)	BET surface area, S_{BET} (m^2/g)	Total pore volume (cm^3/g)	Micropore area (m^2/g)	Pore size (A°)
300	841.3	0.35	661.9	21.3
600	792.5	0.29	619.2	22.7

capacity and longer breakthrough time than AC300µm-[Bmim][NTf_2]-U5. The breakthrough time of AC300µm-[Bmim][NTf_2]-U5 is shorter than AC300µm-[Bmim]Cl-U5, consistently with a lower adsorption capacity of 6.48±0.18 mg H_2S/g. Within 105 minutes of adsorption time, AC300µm-[Bmim]Cl-U5 achieved up to 89.00% removal efficiency of H_2S, while AC300µm-[Bmim][NTf_2]-U5 exhibited lower but still comparable removal efficiency of 87.60%.

In H_2S adsorption, [Bmim]Cl possesses better H_2S selectivity than [Bmim][NTf_2] due to its polar nature, which is mainly associated with imidazolium cation. It was reported that the presence of [Bmim]Cl with 10% loading on silica was more effective than 50% of [Bmim][NTf_2] on the same support material of silica (Bárbara B. Polesso et al., 2019). Other than higher selectivity, fluorinated anions with smaller sizes can provide greater access for adsorption and offer better solubility than larger anions, such as NTf_2^- (Li et al., 2023). In addition, the hydrophilic nature of [Bmim]Cl contributes to its ability to adsorb a high capacity of H_2S. H_2S is known as a weak acid gas. Hence, it is very water-soluble, where the solubility reported to be ~80 mM at 37°C as an equilibrium between molecules (Caglayan et al., 2023; Zhao et al., 2014). Not only that, the IL anion of [Cl^-] performed better selectivity and activity than other anions, such as [BF_4^-], [PF_6^-] and [NTF_2^-] and has stronger nucleophilicity than [Br-] and [I-] (Aquino et al., 2015). Therefore, [Bmim]Cl is strongly recommended for further investigation as an excellent supported ionic liquid adsorbent for H_2S removal.

Thermodynamic characteristic of IL and H_2S

The prediction for gas solubility was conducted through the COSMO-RS computational program. Before the prediction, validating the COSMO-RS using experimental data is crucial to confirm the reliability and accuracy of the model. Hence, the available experimental solubility data were collected from this study and the literature as well as compared against the COSMO-RS predicted solubility values. The experimental and predicted H_2S solubility, Henry's law constant (H) and excess enthalpy (H^E) of six chosen IL from the literature are presented in Table 2. Figure 5a and Figure 5b

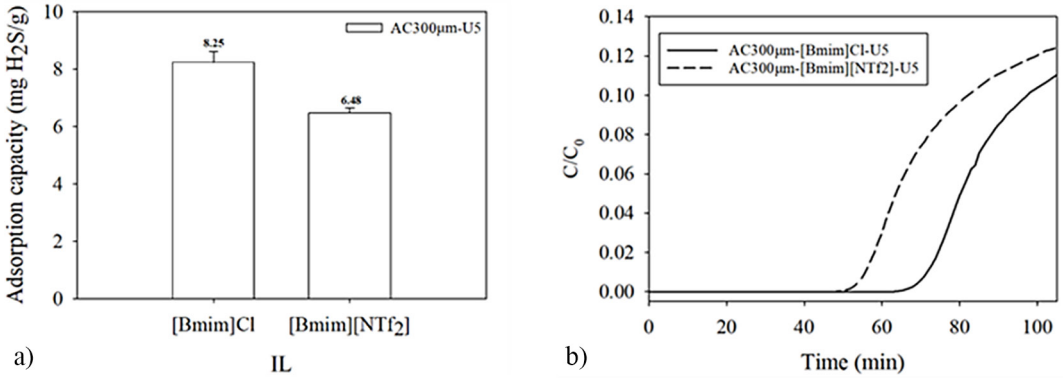

Figure 4. (a) H_2S adsorption capacity and (b) breakthrough curve of AC300-U5 with different IL anion type of [Bmim]Cl and [Bmim]NTf_2 under ambient temperature and pressure

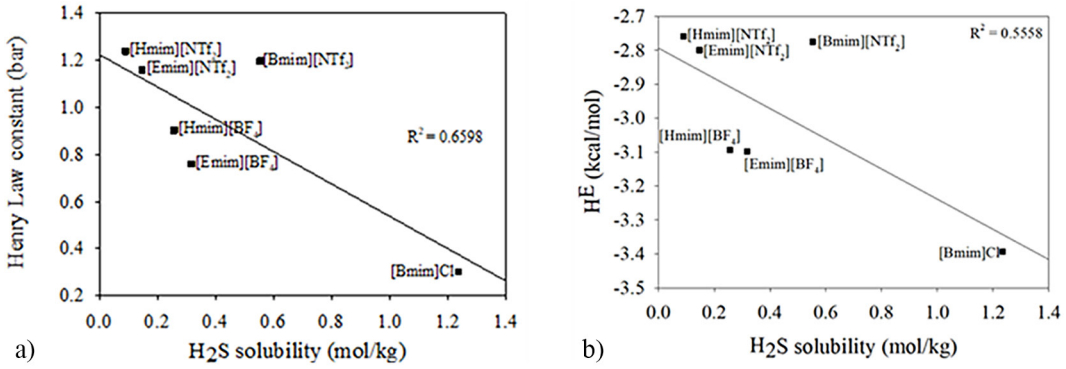

Figure 5. (a) Henry law constant and (b) excess enthalpy against H_2S solubility of six chosen IL

portray the H and H^E against H_2S solubility. It was observed that [Bmim]Cl gave the highest H_2S solubility compared to other imidazolium-based IL at lower H (0.301 bar) and H^E (-3.393 kcal/mol). The lower H and H^E values of the solute in the solvents indicate that the solvent exhibits a high tendency to interact and dissolve the solute (Mohan et al., 2022). The highly electronegative Cl^- significantly enhances the polarity of the whole IL system, thus making it a suitable hydrogen bond acceptor. The R value is considered insignificantly critical aligning with the purpose of the benchmarking study. Therefore, it is believed that [Bmim]Cl can form a strong hydrogen bond with H_2S considering that H_2S inherently is a strong hydrogen-bond donor (Santiago et al., 2020). Unlike NTf_2^- anion, the acidic nature of the anion results in lower interaction with H_2S, given the acidic nature of H_2S itself (Mutalib et al., 2022).

The interactions between the IL and H_2S were analyzed by the σ-profile and σ-potential curves portrayed in Figure 6a and Figure 6b. There are three main regions in σ-profile and σ-potential: hydrogen bond acceptor (σ > 0.01 eÅ²), hydrogen bond donor (σ < -0.01 eÅ²), and nonpolar (-0.01 eÅ² < σ < 0.01 eÅ²). For H_2S, it can be observed that the peaks appear at the range of -0.013 to 0.013 e/Å², in which the polar peaks formed at 0.005 e/Å² and -0.010 e/Å² correspond to S and H atoms, respectively. On the other hand, the curve in the nonpolar region is contributed by the partial screening charge densities between the two S–H bonds. Hence, H_2S can be said to have polar and nonpolar properties. The σ-profile of H_2S is in agreement by the σ-potential where H_2S has the lowest negative value in the hydrogen bond acceptor region, which induces high affinity towards [Bmim]Cl. The σ-profile of [Bmim]Cl falls in the range of -0.017 to 0.020 e/Å², indicating an affinity for the molecules with nonpolar and hydrogen bond acceptor properties. Additionally, the Cl- anion peaks at 0.019 e/Å represent a strong hydrogen bond acceptor capability (Mutalib et al., 2022). The σ-profile is in line with the σ-potential of [Bmim]Cl, in which the Cl^- anion shows strong affinity to hydrogen bond donor, as reflected by the curve of σ >-0.010 e/Å². In addition, $[Bmim]^+$ cation shows a narrow curve with negative μ values on the right side, reflecting a relevant affinity towards a hydrogen bond-accepting molecule, i.e., the S atoms of H_2S. Meanwhile, the σ-profile of $[Bmim][NTf_2]$ falls in the range of -0.017 to 0.016 e/Å², with the largest peak formed at +0.002 e/Å², indicating the strong nonpolar property of the alkyl-fluorine group. The peak of NTf_2^- anion appears at 0.011 e/Å² indicating a weaker affinity to

Table 2. List of experimental and COSMO-RS predicted H_2S solubility, H and H^E of six chosen IL at 1 bar

IL	Experimental H_2S solubility (mol/kg)	Predicted H_2S solubility (mol/mol)	H (bar)	H^E (kcal/mol)
[Bmim]Cl	1.234[e]	0.6500	0.3012	-3.39355
$[Bmim][NTf_2]$	0.5525[e]	0.5400	1.1963	-2.77514
$[Hmim][NTf_2]$	0.0894	0.5400	1.2370	-2.75885
$[Emim][NTf_2]$	0.1465	0.3782	1.1586	-2.79958
$[Hmim][BF_4]$	0.2565	0.4114	0.9023	-3.09337
$[Emim][BF_4]$	0.3170	0.3937	0.7585	-3.09767

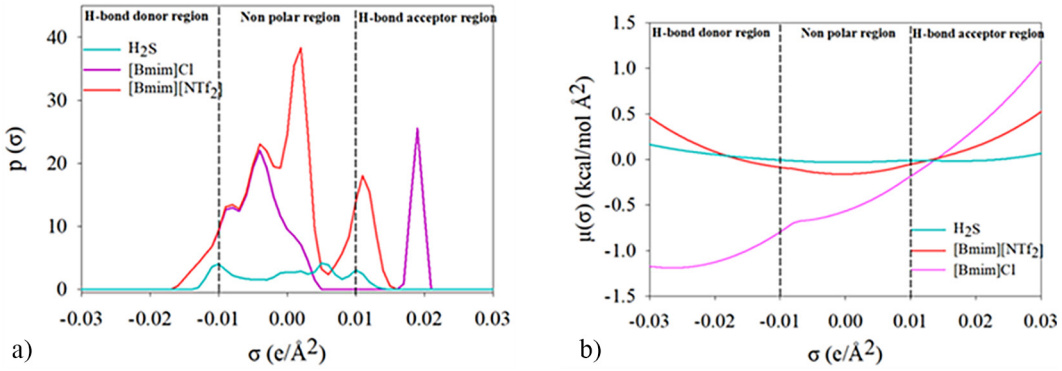

Figure 6. (a) σ-profile and (b) σ-potential of [Bmim]Cl, $[Bmim][NTf_2]$ and H_2S

hydrogen bond acceptor than Cl^-. This is consistent with the σ-potential of NTf_2^- anion at the value of -0.009 e/Å^2 illustrating the affinity toward hydrogen bond donor and rejecting hydrogen bond acceptor molecule (Azlan Kassim et al., 2020).

Regeneration study

The regeneration study involved assessing adsorption capacity until saturation by the chosen adsorbent, AC300µm-[Bmim]Cl-U5. Desorption of the exhausted adsorbent was conducted at 150°C for 30 minutes. The adsorption/desorption profile, depicted in the Figure 7a revealed that AC300µm-[Bmim]Cl-U5 reached the saturation point at the same C/C_0 ratio for the first three cycles. Although the total adsorption time spanned 690 minutes, the adsorption time for cycles 1 to 3 at $C/C_0 = 0$ gradually shortened. This indicates a decrease in durability, aligning with the Q_{max} values in the Figure 7b and Table 3.

Calculation using Equation 2 revealed a high Q_{max} of 14.24 mg H_2S/g in the first cycle as presented in Figure 7b, attributed to the presence of pores and the number of active sites on the AC surface. However, the degradation percentage was 42.25%, with an adsorption time of 35 minutes at $C/C_0 = 0$, shorter than in the first cycle (65 minutes). Throughout the adsorption/desorption tests, the degradation percentage stays on average between 33.17% and 42.25%, indicative of a decreasing effectiveness of the adsorbent.

Therefore, optimising regeneration conditions, such as temperature and heating time, becomes crucial for prolonging the shelf life of this adsorbent. In conclusion, AC300µm-[Bmim]Cl-U5 demonstrated the potential for regeneration through heating at 150 °C for 30 minutes for at least three cycles, with an acceptable reduction in Q_{max} as observed in previous studies (Ma et al., 2019).

Physicochemical characteristic

XRD

The analysis of crystallinity and amorphous properties was conducted on various samples, including raw AC, fresh and exhausted adsorbents, AC300µm, AC300µm-[Bmim]Cl-U5(B), and AC300µm-[Bmim]Cl-U5. The high carbon peak (002) at 2θ = 24° indicates the amorphous structure of carbon, while the broad peak signifies the positive impact of effective IL dispersion on the AC surface. Table 4 revealed that AC300µm, in its pristine state without impregnation, exhibits amorphous characteristics with a

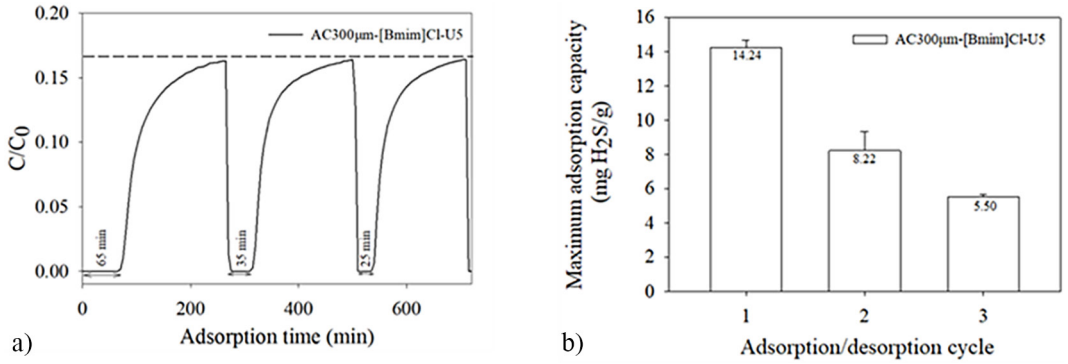

Figure 7. (a) Profile and (b) maximum adsorption capacity of three H_2S adsorption/desorption cycle of AC300µm-[Bmim]Cl-U5

Table 3. Adsorption time, maximum adsorption capacity, and degradation percentage of AC300µm-[Bmim]Cl-U5 for each cycle

Adsorption/desorption cycle	Adsorption time at 1 ppm (min)	Maximum adsorption capacity, Q_{max} (mg H_2S/g)	Degradation (%)
1	65	14.24±0.43	0
2	35	8.22±1.14	42.25
3	25	5.50±0.16	33.17

Table 4. Percentage and ratio of amorphous (A) and crystallinity (C) of AC-300µm, AC300µm-[Bmim]Cl-U5(B) and AC300µm-[Bmim]Cl-U5

Material	Amorphous (%)	Crystallinity (%)	Ratio amorphous: crystallinity
AC300µm	71.1	28.9	2.46:1.00
AC300µm-[Bmim]Cl-U5(B)	52.6	47.4	1.10:1.00
AC300µm-[Bmim]Cl-U5	50.5	49.5	1.02:1.00

71.1% and Amorphous: Crystallinity (A: C) ratio of 2.26:1.00. In contrast, the fresh and exhausted adsorbents of AC300µm-[Bmim]Cl-U5(B) and AC300µm-[Bmim]Cl-U5 display A: C ratios of 1.10:1.00 and 1.02:1.00, respectively.

The crystallinity properties of AC300µm-[Bmim]Cl-U5 are notably enhanced compared to the pristine AC300µm, primarily attributed to the ultrasonic stirring effect applied during the impregnation process. The high-frequency vibrations generated by ultrasonic waves have effectively modified the crystallinity of AC. Dou et al. (2016) agreed that ultrasonic radiation strongly effects adsorbent properties by promoting the impregnation process and increasing the crystallisation of the particles. The higher crystallinity percentage of AC300µm-[Bmim]Cl-U5(B) proved the even dispersion of IL active component on the AC surface, which has positively affected the adsorption capacity (Dou et al., 2015).

SEM-EDX

The SEM images in Figure 8 demonstrated the morphological structures of AC300µm-[Bmim]Cl-U5(B) and AC300µm-[Bmim]Cl-U5. A white composition is observed along the surface walls and within the pores. This observation aligns with the expected distribution of IL composition on the AC surfaces which was achieved by applying ultrasonic stirring. The particles of [Bmim]

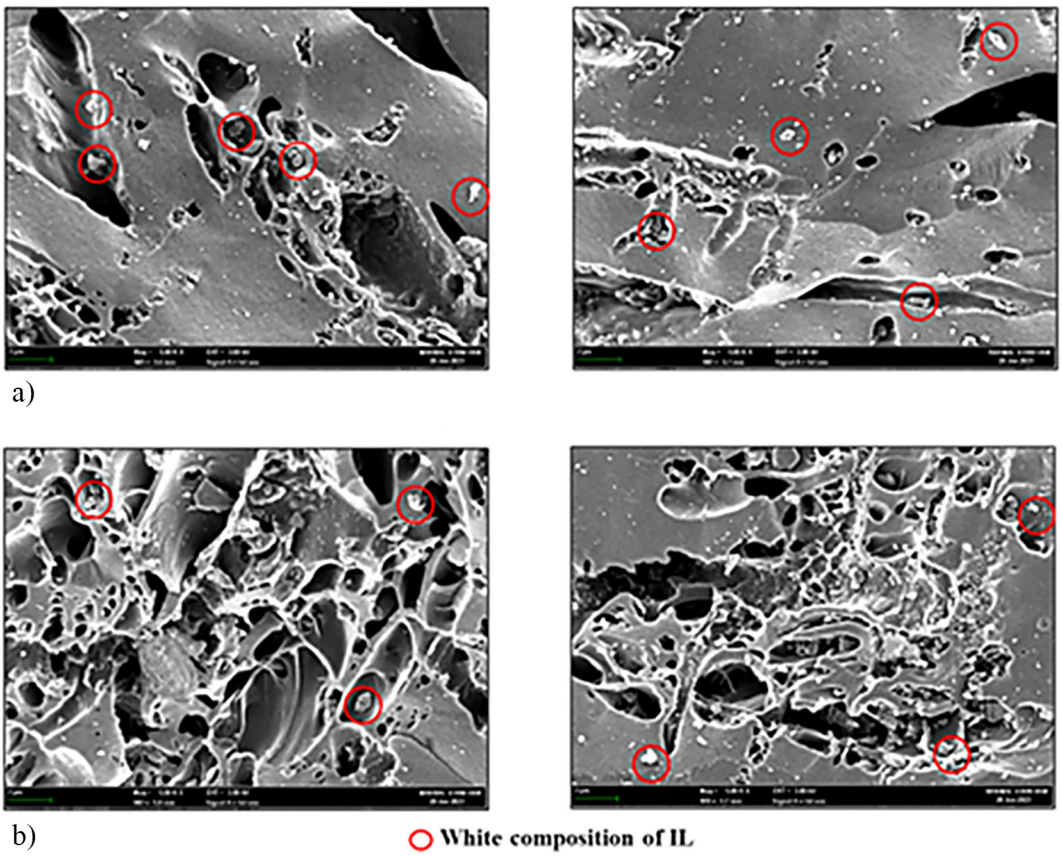

Figure 8. The morphology of (a) AC300µm-[Bmim]Cl-U5(B) and (b) AC300µm-[Bmim]Cl-U5 at the magnification scale of 5.0 Kx (2µm)

Cl exhibited uniform and deeper adherence to the AC particles. Consequently, this short five-minute ultrasonic stirring process effectively avoided IL leaching from the AC surface. After the H_2S adsorption test, the surface of AC300µm-[Bmim]Cl-U5 reveals the presence of adsorbed sulphur gas within its pores. Table 5 indicates the composition in weight percentage (wt %) for each element in the H_2S adsorbent. AC-[Bmim]Cl-U5 exhibited an average sulphur adsorption of 3.70 wt % which indicated increased surface area and pore volume. AC300µm-[Bmim]Cl-U5(B) recorded a high impregnation of 2.5 wt % Cl on the AC surface and this has highlighted the effectiveness of the ultrasonic stirring method in achieving a well-distributed dispersion of IL on the AC surface.

BET

According to the IUPAC classification of pore dimensions, pores are categorised into three types: micropores (d < 2 nm), mesopores (d = 2–50 nm), and macropores (d > 50 nm) (Thommes et al., 2015). The AC300µm-[Bmim]Cl-U5 adsorbent falls under the micropore category with a size below 2 nm. Micropore adsorbents are well-known as excellent materials of choice for the adsorption of H_2S, as conducted in a previous study (Chaves and Jiménez, 2018). Table 6 shows a reduction in the surface area value of AC300µm-[Bmim]Cl-U5(B), decreasing from 583.00 to 540.99 m^2/g as adsorption occurs. Specifically, the micropore area decreases from 460.54 m^2/g before adsorption to 400.52 m^2/g after adsorption, indicating a 13.03% reduction due to gas content filling the pores. These reductions in surface area and pore volume align with the findings from a previous study (Choo et al., 2013). The N_2 adsorption-desorption method is employed to determine the adsorption type and the pore structure of the adsorbent. The N_2 adsorption profile reveals a Type 1 isotherm (IUPAC), signifying multilayer adsorption on micropore adsorbents (Thommes et al., 2015). Both the AC300µm-[Bmim]Cl-U5(B) and AC300µm-[Bmim]Cl-U5 samples exhibit similar behaviour, as evidenced by the graph lines. Apart from the information presented in Table 6, these materials distinctly showcase their micropore properties, particularly in the low relative pressure range ($p/p_0 < 0.1$). Regarding N_2 adsorption, AC300µm-[Bmim]Cl-U5(B) demonstrates a high adsorption quantity, reaching up to 190 cm^3/g STP. Similarly, AC300µm-[Bmim]Cl-U5 maintains a significant adsorption capacity, even after H_2S adsorption, with the ability to adsorb up to 175 cm^3/g STP.

TGA

The TGA and DTG profiles of AC300µm-[Bmim]Cl-U5(B), AC300µm-[Bmim]Cl-U5, and [Bmim]Cl are presented in Figure 9a and Figure 9b, showcasing the temperature derivative from room temperature to 600 °C at a heating rate of 20°C/min in a nitrogen atmosphere. Mass losses and their rate were meticulously recorded across temperature derivatives of 30–100 °C, 100–400 °C, and 400–600°C in Figure 9a and Figure 9b as well as detailed in Table 7 below. Notably, in the 100–400 °C temperature range, AC300µm-[Bmim]Cl-U5(B), AC300µm-[Bmim]Cl-U5, and [Bmim]Cl exhibited the highest mass losses compared to the derivative of 400–600 °C and 30–100 °C. The mass loss of the prepared adsorbent, AC300µm-[Bmim]Cl-U5, is substantially lower than that of the pure IL, [Bmim]Cl and the mass loss rate (%/min) of AC300µm-[Bmim]Cl-U5 is higher compared to [Bmim]Cl. This can be attributed to the successful impregnation effect, which synergistically combines the unique properties of AC and IL and leads to higher H_2S

Table 5. EDX analysis of AC300µm-[Bmim]Cl-U5(B) and AC300µm-[Bmim]Cl-U5

H_2S adsorbents	C (wt %)	Cl (wt %)	S (wt %)
AC300µm-[Bmim]Cl-U5(B)	97.50	2.50	0.00
AC300µm [Bmim]Cl-U5	90.80	5.30	3.70

Table 6. Pore properties of AC300µm-[Bmim]Cl-U5(B) and AC300µm-[Bmim]Cl-U5

Materials	BET Surface area, S_{BET} (m^2/g)	Total pore volume (cm^3/g)	Micropore area (m^2/g)	Pore size (A°)
AC300µm-[Bmim]Cl-U5(B)	583.00	0.22	460.54	19.95
AC300µm-[Bmim]Cl-U5	540.99	0.20	400.52	19.82

Table 7. Mass loss (%) for temperature derivative of AC300µm-[Bmim]Cl-U5(B), AC300µm-[Bmim]Cl-U5 and [Bmim]Cl

Temperature derivatives (°C)	AC300µm-[Bmim]Cl-U5(B)	AC300µm-[Bmim]Cl-U5	[Bmim]Cl
	Mass loss (%)		
30–100	1.04	0.91	2.64
100–400	8.83	8.74	9.75
400–600	2.56	2.54	2.44

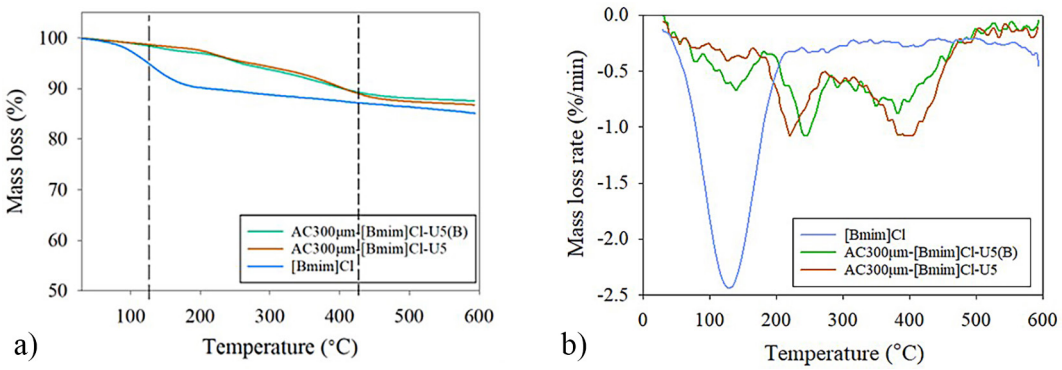

Figure 9. Profile analysis of (a) TGA and (b) DTG of AC300µm-[Bmim]Cl-U5(B), AC300µm-[Bmim]Cl-U5 and [Bmim]Cl at temperature range of 30–600°C

adsorption capacity. Consequently, the thermal stability of this H_2S adsorbent has markedly improved, proven by a low degradation rate ranging from 0.91% to 8.74% (Table 7). However, Zulkefli et al. (2019) produced an H_2S adsorbent from $ZnAc_2$-AC, exhibiting a higher mass loss ranging from 4–16% at the initial temperature derivatives of 29–100°C. It is acknowledged that this temperature range is usually associated with moisture loss inherent in the adsorbents. The actual IL loading (%) on AC can also be calculated from this analysis through Equation 6 below, and it revealed that a high amount of 76.7% IL was successfully impregnated on the AC surface.

$$[\text{Bmim}]\text{Cl}\ (\%) = (W_{100} - W_{600})/W_{100} \times 100 \quad (6)$$

where: W_{100} and W_{600} – represent the mass (g) at temperatures of 100°C and 600°C, respectively.

CONCLUSIONS

AC-IL adsorbents were successfully synthesized through ultrasonic stirring at room temperature. Characterisation using XRD, SEM-EDX, BET, and N_2-sorption analyses confirmed the successful impregnation of IL onto AC and revealed the contrasts between the fresh and exhausted adsorbents. In terms of adsorption capacity, the pairing of AC300µm with [Bmim]Cl exhibited superior performance compared to [Bmim][NTf_2]. The COSMO-RS study emphasises the super H_2S solubility of [Bmim]Cl relative to [Bmim][NTf_2] and other ILs under consideration. Consequently, AC300µm-[Bmim]Cl-U5 emerged as the most effective adsorbent, performing the highest adsorption capacity and good regeneration capability. Remarkably, with only five minutes of stirring time and without additional heating, AC300µm-[Bmim]Cl-U5 demonstrated the ability to adsorb up to 8.25 ±0.38 mg H_2S/g. Furthermore, it exhibits the capability for regeneration through at least three cycles with acceptable degradation and demonstrates stability in the adsorption profile throughout each cycle. AC300µm-[Bmim]Cl-U5 achieved an impressive 83.7% H_2S removal efficiency, decreasing the concentration from 2000 to 326 ppm in the first cycle. These findings validate the synthesis approach and highlight the excellent adsorption performance as well as high removal efficiency of AC300µm-[Bmim]Cl-U5 as a promising candidate for H_2S removal applications.

Acknowledgements

We gratefully acknowledge the financial and technical support provided by the Universiti Kebangsaan Malaysia-Yayasan Sime Darby

(UKM-YSD) Chair for Sustainability. We would also like to thank the Government of Malaysia and Universiti Kebangsaan Malaysia for funding this work through Malaysia Research University Network (MRUN) Grant (LRGS MRUN/F2/01/2019/4/2).

REFERENCES

1. Al Mamun, M.R., Torii, S. 2015. Enhancement of production and upgradation of biogas using different techniques- a review. Int. J. Earth Sci. Eng. 8, 877–892.
2. Amin, M.A., Shukor, H., Yin, L.S., Kasim, F.H., Shoparwe, N.F., Makhtar, M.M.Z., Yaser, A.Z. 2022. Methane biogas production in Malaysia: challenge and future plan. Int. J. Chem. Eng. 2022. https://doi.org/10.1155/2022/2278211
3. Andriani, D., Rajani, A., Kusnadi, Santosa, A., Saepudin, A., Wresta, A., Atmaja, T.D. 2020. A review on biogas purification through hydrogen sulphide removal. IOP Conf. Ser. Earth Environ. Sci. 483. https://doi.org/10.1088/1755-1315/483/1/012034
4. Aquino, A.S., Bernard, F.L., Borges, J. V., Mafra, L., Vecchia, F.D., Vieira, M.O., Ligabue, R., Seferin, M., Chaban, V. V., Cabrita, E.J., Einloft, S. 2015. Rationalizing the role of the anion in CO2 capture and conversion using imidazolium-based ionic liquid modified mesoporous silica. RSC Adv. 5, 64220–64227. https://doi.org/10.1039/c5ra07561k
5. Azlan Kassim, M., Asrina Sairi, N., Yusoff, R., Kheireddine Aroua, M. 2020. Experimental Densities of Binary mixture of 1-butyl-3-methylimidazolium bis(trifluoromethylsulfonyl)imide or sulfolane with monoethanolamine and their molecular interaction by COSMO-RS. IOP Conf. Ser. Mater. Sci. Eng. 778. https://doi.org/10.1088/1757-899X/778/1/012022
6. Balchandani, S., Singh, R. 2021. COSMO-RS Analysis of CO_2 Solubility in N-Methyldiethanolamine, Sulfolane, and 1-Butyl-3-methyl-imidazolium Acetate Activated by 2-Methylpiperazine for Postcombustion Carbon Capture. ACS Omega 6, 747–761. https://doi.org/10.1021/acsomega.0c05298
7. Beigi, A.A.M., Yousefi, M., Abdouss, M., 2018. Room temperature imidazolium-based ionic liquids as scavengers for hydrogen sulfide removal of crude oil. Anal. Methods Environ. Chem. J. 1, 11–22. https://doi.org/10.24200/amecj.v1.i01.32
8. Caglayan, H.P., Unal, U., Keskin, S., Uzun, A. 2023. Effect of Surface Characteristics of Graphene Aerogels and Hydrophilicity of Ionic Liquids on the CO_2/CH_4 Separation Performance of Ionic Liquid/Reduced Graphene Aerogel Composites. ACS Appl. Nano Mater. 6, 2203–2217. https://doi.org/10.1021/acsanm.2c05476
9. Chaemchuen, S., Zhou, K., Verpoort, F. 2016. From biogas to biofuel: Materials used for biogas cleaning to biomethane. ChemBioEng Rev. 3, 250–265. https://doi.org/10.1002/CBEN.201600016/PDF
10. Chaves, F.A., Jiménez, D. 2018. Effect of Impregnated Activated Carbon on Carbon Dioxide Adsorption Performance for Biohydrogen Purification. Nanotechnology 29.
11. Cheng, H., Li, N., Zhang, R., Wang, N., Yang, Y., Teng, Y., Jia, W., Zheng, S. 2021. Measuring and modeling the solubility of hydrogen sulfide in rFeCl3/[bmim]Cl. Processes 9, 1–13. https://doi.org/10.3390/pr9040652
12. Choi, S.Y., Nam, S.C., Yoon, Y. Il, Park, K.T., Park, S.J. 2014. Carbon dioxide absorption into aqueous blends of methyldiethanolamine (MDEA) and alkyl amines containing multiple amino groups. Ind. Eng. Chem. Res. 53, 14451–14461. https://doi.org/10.1021/ie502434m
13. Choo, H.S., Lau, L.C., Mohamed, A.R., Lee, K.T. 2013. Hydrogen sulfide adsorption by alkaline impregnated coconut shell activated carbon. J. Eng. Sci. Technol. 8, 741–753.
14. Dou, J., Tahmasebi, A., Li, X., Yin, F., Yu, J. 2016. Char-supported Fe-Zn-Cu sorbent prepared by ultrasonic-assisted impregnation for simultaneous removal of H_2S and COS from coke oven gas. Environ. Prog. Sustain. Energy 35, 352–358. https://doi.org/10.1002/ep.12224
15. Dou, J., Yu, J., Tahmasebi, A., Yin, F., Gupta, S., Li, X., Lucas, J., Na, C., Wall, T. 2015. Ultrasonic-assisted preparation of highly reactive Fe-Zn sorbents supported on activated-char for desulfurization of COG. Fuel Process. Technol. 135, 187–194. https://doi.org/10.1016/j.fuproc.2015.01.035
16. Duczinski, R., Bernard, F., Rojas, M., Duarte, E., Chaban, V., Vecchia, F.D., Menezes, S., Einloft, S. 2018. Waste derived MCMRH- supported IL for CO2/CH4 separation. J. Nat. Gas Sci. Eng. 54, 54–64. https://doi.org/10.1016/j.jngse.2018.03.028
17. Guanhua, N., Zhao, L., Qian, S., Shang, L., Kai, D. 2019. Effects of [Bmim][Cl] ionic liquid with different concentrations on the functional groups and wettability of coal. Adv. Powder Technol. 30, 610–624. https://doi.org/10.1016/j.apt.2018.12.008
18. Huang, K., Feng, X., Zhang, X.M., Wu, Y.T., Hu, X.B. 2016. The ionic liquid-mediated Claus reaction: A highly efficient capture and conversion of hydrogen sulfide. Green Chem. 18, 1859–1863. https://doi.org/10.1039/c5gc03016a
19. Huang, Z., Mohamedali, M., Karami, D., Mahinpey, N. 2022. Evaluation of supported multi-functionalized amino acid ionic liquid-based sorbents for low temperature CO2 capture. Fuel 310, 122284. https://doi.org/10.1016/j.fuel.2021.122284
20. Jalili, A.H., Rahmati-Rostami, M., Ghotbi, C.,

Hosseini-Jenab, M., Ahmadi, A.N. 2009. Solubility of H_2S in ionic liquids [bmim][PF6], [bmim][BF4], and [bmim][Tf2N]. J. Chem. Eng. Data 54, 1844–1849. https://doi.org/10.1021/je8009495

21. Jalili, A.H., Shokouhi, M., Maurer, G., Zoghi, A.T., Sadeghzah Ahari, J., Forsat, K. 2019. Measuring and modelling the absorption and volumetric properties of CO_2 and H_2S in the ionic liquid 1-ethyl-3-methylimidazolium tetrafluoroborate. J. Chem. Thermodyn. 131, 544–556. https://doi.org/10.1016/j.jct.2018.12.005
22. Jiang, B., Zhang, J., Chen, Y., Song, H., Hao, T., Kuang, J. 2020. Ultrasonic-assisted preparation of highly active Co_3O_4/MCM-41 adsorbent and its desulfurization performance for low H_2S concentration gas. RSC Adv. 10, 30214–30222. https://doi.org/10.1039/d0ra05606e
23. Kalidhasan, S., Santhana KrishnaKumar, A., Rajesh, V., Rajesh, N. 2012. Ultrasound-assisted preparation and characterization of crystalline cellulose-ionic liquid blend polymeric material: A prelude to the study of its application toward the effective adsorption of chromium. J. Colloid Interface Sci. 367, 398–408. https://doi.org/10.1016/j.jcis.2011.09.062
24. Korbag, I., Mohamed Saleh Omer, S., Boghazala, H., Ahmeedah Aboubakr Abusasiyah, M. 2021. Recent advances of biogas production and future perspective. Biogas - Recent Adv. Integr. Approaches. https://doi.org/10.5772/intechopen.93231
25. Li, W., Xiao, W., Luo, Q., Yan, J., Zhang, G., Chen, L., Sun, J. 2023. Ionic liquids promoted synthesis, enhanced functions, and expanded applications of porous organic frameworks. Coord. Chem. Rev. 493, 215304. https://doi.org/10.1016/j.ccr.2023.215304
26. Ma, Y., Mao, J., Xiao, C., Li, Y., Zang, L. 2019. Immobilization of functionalized ionic liquid on sol-gel derived silica for efficient removal of H_2S. China Pet. Process. Petrochemical Technol. 21, 62–70.
27. Mohan, M., Keasling, J.D., Simmons, B.A., Singh, S. 2022. In silico COSMO-RS predictive screening of ionic liquids for the dissolution of plastic. Green Chem. 24, 4140–4152. https://doi.org/10.1039/d1gc03464b
28. Mullick, A., Neogi, S. 2019. Ultrasound assisted synthesis of Mg-Mn-Zr impregnated activated carbon for effective fluoride adsorption from water. Ultrason. Sonochem. 50, 126–137. https://doi.org/10.1016/j.ultsonch.2018.09.010
29. Mutalib, N.F.A., Bustam, M.A., Wirzal, M.D.H., Idris A. 2022. A prediction for the conversion performance of H_2S to elemental sulfur in an ionic-liquid-incorporated transition metal using COSMO-RS. Chemistry, 4(3), 811–826. https://doi.org/10.3390/chemistry4030058
30. Nurhidayah, A., Zaini, N., Zulhaziman, M., Salleh, M., Zulbadli, N., Mohamad, N.A., Ezaty, S.N., Shafie, N.S., Sahri, D.M., Mohd Najib, S.S.A. 2022. Evaluation of physically modified kenaf core adsorbent for carbon dioxide adsorptive study. J. Phys. Conf. Ser. 2259. https://doi.org/10.1088/1742-6596/2259/1/012007
31. Lucena P., S.M., Angel Centeno, M., Rios, R., Juliano Prauchner marcosjp, M., Juliano Prauchner, M., da Cunha Oliveira, S., Rodríguez-Reinoso, F. 2020. Tailoring low-cost granular activated carbons Intended for CO_2 adsorption. Front. Chem. | www.frontiersin.org 8, 581133. https://doi.org/10.3389/fchem.2020.581133
32. Plaza, M.G., García, S., Rubiera, F., Pis, J.J., Pevida, C. 2010. Post-combustion CO_2 capture with a commercial activated carbon: Comparison of different regeneration strategies. Chem. Eng. J. 163, 41–47. https://doi.org/10.1016/j.cej.2010.07.030
33. Polesso, Bárbara B., Bernard, F.L., Ferrari, H.Z., Duarte, E.A., Vecchia, F.D., Einloft, S. 2019. Supported ionic liquids as highly efficient and low-cost material for CO_2/CH_4 separation process. Heliyon 5. https://doi.org/10.1016/j.heliyon.2019.e02183
34. Polesso, Bárbara Burlini, Duczinski, R., Bernard, F.L., Ferrari, H.Z., Da Luz, M., Vecchia, F.D., De Menezes, S.M.C., Einloft, S. 2019. Imidazolium-based ionic liquids impregnated in silica and alumina supports for CO2 capture. Mater. Res. 22, 1–10. https://doi.org/10.1590/1980-5373-MR-2018-0810
35. Prasad, S., Rathore, D., Singh, A. 2017. Recent Advances in Biogas Production. Chem Eng Process Tech 3, 1038.
36. Rahmati-Rostami, M., Ghotbi, C., Hosseini-Jenab, M., Ahmadi, A.N., Jalili, A.H. 2009. Solubility of H_2S in ionic liquids [hmim][PF6], [hmim][BF4], and [hmim][Tf2N]. J. Chem. Thermodyn. 41, 1052–1055. https://doi.org/10.1016/j.jct.2009.04.014
37. Ren, H., Li, H., Shen, H., Liu, Y. 2023. Experimental study on CO_2 adsorption with silica-supported ionic liquid in a high gravity reactor. Fuel 331, 125932. https://doi.org/10.1016/j.fuel.2022.125932
38. Ren, H., Shen, H., Liu, Y. 2022. Adsorption of CO_2 with tetraethylammonium glycine ionic liquid modified alumina in the Rotating Adsorption Bed. J. CO_2 Util. 58, 101925. https://doi.org/10.1016/j.jcou.2022.101925
39. Sakhaeinia, H., Jalili, A.H., Taghikhani, V., Safekordi, A.A., Ahmadi, A.N. 2010. Solubility of H_2S in Ionic Liquids 1-Ethyl-3-methylimidazolium Hexafluorophosphate ([emim][PF6]) and 1-Ethyl-3-methylimidazolium Bis(trifluoromethyl)sulfonylimide ([emim][Tf2N]) Hossein. J. Chem. Eng. Data 55, 5839–5845.
40. Santiago, R., Lemus, J., Hospital-Benito, D., Moya, C., Bedia, J., Alonso-Morales, N., Rodriguez, J.J., Palomar, J. 2019. CO_2 capture by supported ionic liquid phase: Highlighting the role of the particle size. ACS Sustain. Chem. Eng. 7, 13089–13097.

https://doi.org/10.1021/acssuschemeng.9b02277

41. Santiago, R., Lemus, J., Outomuro, A.X., Bedia, J., Palomar, J. 2020. Assessment of ionic liquids as H_2S physical absorbents by thermodynamic and kinetic analysis based on process simulation. Sep. Purif. Technol. 233, 116050. https://doi.org/10.1016/j.seppur.2019.116050
42. Syahri, S.N.K.M., Hasan, H.A., Abdullah, S.R.S., Othman, A.R., Abdul, P.M., Azmy, R.F.H.R., Muhamad, M.H. 2022. Recent Challenges of Biogas Production and its Conversion to Electrical Energy. J. Ecol. Eng. 23, 251–269. https://doi.org/10.12911/22998993/146132
43. Taheri, M., Zhu, R., Yu, G., Lei, Z. 2021. Ionic liquid screening for CO_2 capture and H_2S removal from gases: The syngas purification case. Chem. Eng. Sci. 230, 116199. https://doi.org/10.1016/j.ces.2020.116199
44. Thommes, M., Kaneko, K., Neimark, A.V., Olivier, J.P., Rodriguez-Reinoso, F., Rouquerol, J., Sing, K.S.W. 2015. Physisorption of gases, with special reference to the evaluation of surface area and pore size distribution (IUPAC Technical Report). Pure Appl. Chem. 87, 1051–1069. https://doi.org/10.1515/pac-2014-1117
45. Xiao, C. 2017. Review of desulfurization process for biogas purification. IOP Conf. Ser. Earth Environ. Sci. 100. https://doi.org/10.1088/1755-1315/100/1/012177
46. Zhang, H.Y., Yang, C., Geng, Q., Fan, H.L., Wang, B.J., Wu, M.M., Tian, Z. 2019. Adsorption of hydrogen sulfide by amine-functionalized metal organic framework (MOF-199): An experimental and simulation study. Appl. Surf. Sci. 497, 143815. https://doi.org/10.1016/j.apsusc.2019.143815
47. Zhang, J., Song, H., Chen, Y., Hao, T., Li, F., Yuan, D., Wang, X., Zhao, L., Gao, J. 2018. Amino-modified molecular sieves for adsorptive removal of H_2S from natural gas. RSC Adv. 8, 38124–38130. https://doi.org/10.1039/c8ra06859c
48. Zhang, Z., Liu, X., Li, D., Lei, Y., Gao, T., Wu, B., Zhao, J., Wang, Y., Zhou, G., Yao, H. 2019. Mechanism of ultrasonic impregnation on porosity of activated carbons in non-cavitation and cavitation regimes. Ultrason. Sonochem. 51, 206–213. https://doi.org/10.1016/j.ultsonch.2018.10.024
49. Zhao, Y., Biggs, T.D., Xian, M. 2014. Hydrogen sulfide (H_2S) releasing agents: chemistry and biological applications. ChemInform 45, 11788–11805. https://doi.org/10.1039/c4cc00968a
50. Zhou, X., Cao, B., Liu, S., Sun, X., Zhu, X., Fu, H. 2016. Theoretical and experimental investigation on the capture of H_2S in a series of ionic liquids. J. Mol. Graph. Model. 68, 87–94. https://doi.org/10.1016/j.jmgm.2016.06.013
51. Zulkefli, N.N., Mathuray Veeran, L.S., Noor Azam, A.M.I., Masdar, M.S., Wan Isahak, W.N.R. 2022a. Effect of bimetallic-activated carbon impregnation on adsorption–desorption performance for hydrogen sulfide (H_2S) capture. Materials (Basel). 15, 5409. https://doi.org/10.3390/ma15155409
52. Zulkefli, N.N., Seladorai, R., Masdar, M.S., Sofian, N.M., Isahak, W.N.R.W. 2022b. Core Shell Nanostructure: Impregnated Activated Carbon as Adsorbent for Hydrogen Sulfide Adsorption. Molecules 27, 1–15. https://doi.org/10.3390/molecules27031145
53. Zulkefli, N.N., Shahbudin, M., Id, M., Nor, W., Wan, R., Jahim, J., Rejab, S.A., Lye, C.C. 2019. Removal of hydrogen sulfide from a biogas mimic by using impregnated activated carbon adsorbent. PLoS One, 14(2): e0211713. https://doi.org/10.1371/journal.pone.0211713